Mon. Not. R. Astron. Soc. **378,** 995–1006 (2007) doi:10.1111/j.1365-2966.2007.11842.x

A deep Giant Metre-wave Radio Telescope 610-MHz survey of the 1^H *XMM–Newton*/*Chandra* survey field

D. Moss,[1⋆] N. Seymour,[2] I. M. McHardy,[1] T. Dwelly,[1] M. J. Page[3] and N. S. Loaring [4]

[1]*School of Physics and Astronomy, University of Southampton, Highfield, Southampton SO17 1BJ*
[2]*Spitzer Science Center, California Institute of Technology, Pasadena, CA 91125, USA*
[3]*Mullard Space Science Laboratory, University College London, Holmbury St Mary, Dorking RH5 6NT*
[4]*SAAO, PO Box 9, Observatory, 7935, South Africa*

Accepted 2007 April 5. Received 2007 March 30; in original form 2006 September 8

ABSTRACT

We present the results of a deep 610-MHz survey of the 1^H *XMM–Newton*/*Chandra* survey area with the Giant Metre-wave Radio Telescope. The resulting maps have a resolution of ∼7 arcsec and an rms noise limit of 60 μJy. To a 5σ detection limit of 300 μJy, we detect 223 sources within a survey area of 64 arcmin in diameter. We compute the 610-MHz source counts and compare them to those measured at other radio wavelengths. The well-known flattening of the Euclidean-normalized 1.4-GHz source counts below ∼2 mJy, usually explained by a population of starburst galaxies undergoing luminosity evolution, is seen at 610 MHz. The 610-MHz source counts can be modelled by the same populations that explain the 1.4-GHz source counts, assuming a spectral index of −0.7 for the starburst galaxies and the steep spectrum active galactic nucleus (AGN) population. We find a similar dependence of luminosity evolution on redshift for the starburst galaxies at 610 MHz as is found at 1.4 GHz (i.e. 'Q' $= 2.45^{+0.3}_{-0.4}$).

Key words: surveys – galaxies: active – galaxies: starburst – radio continuum: galaxies.

1 INTRODUCTION

Deep radio surveys provide the basic observational data, that is, counts of the number of sources as a function of radio flux density, on which our understanding of the evolution of the radio source population in the Universe is based (e.g. Longair 1966; Rowan-Robinson et al. 1993; Hopkins et al. 1998; Richards 2000; Seymour, McHardy & Gunn 2004; Huynh et al. 2005). They have thus been the subject of considerable observational effort, particularly at frequencies of 1.4 GHz and above, where angular resolution of a few arcsec or better, is now commonplace and source confusion is unimportant. Radio surveys are also forming an increasingly important part of multiwaveband observational programmes designed to study, in a more holistic manner, the broad-band evolution of various classes of sources such as active galactic nucleus (AGN) and starburst galaxies. At low frequencies (i.e. below 1.4 GHz), where steep spectrum sources such as starburst galaxies are expected to make a larger contribution relative to flatter spectrum AGN, radio surveys have, until recently, been limited to relatively bright flux limits (∼2.5 mJy, Valentijn 1980). This has been primarily due to the lack of a radio telescope with the sensitivity and angular resolution required to reach to faint flux densities without being limited by source confusion. However, the Giant Metre-wave Radio Telescope (GMRT) of India's National Centre for Radio Astrophysics now provides the necessary capabilities at low frequency.

In recent years, a number of deep radio surveys at 1.4 GHz have reached μJy levels (e.g. Hopkins et al. 1998; Richards 2000; Ivison et al. 2002; Seymour et al. 2004; Huynh et al. 2005). They confirmed the previous result (Windhorst et al. 1985) of an upturn in the Euclidean-normalized differential source counts below ∼2 mJy. It is postulated that this upturn is due to a population of sources other than AGN, and is commonly ascribed to starburst galaxies (e.g. Condon 1989; Benn et al. 1993). The source counts have been modelled with a combination of an AGN population (e.g. Dunlop & Peacock 1990) and a starburst population, both undergoing luminosity evolution (e.g. Hopkins et al. 1998).

The previous deepest radio surveys at 610 MHz were made with the Westerbork Synthesis Radio Telescope (WSRT) in the 1970s. Katgert (1979) combined several such surveys to compute source counts down to 22 mJy. Later WSRT surveys of galaxy clusters achieved lower detection limits (e.g. 2.5 mJy, Valentijn 1980). However, none of these surveys was sufficiently deep to reveal the upturn in the source counts.

Here, using GMRT observations, we present a deep 610-MHz survey of a survey field (at 1^h, -4°), which is one of the two very deep survey fields which we have observed in the X-ray, optical and infrared bands, as well as at 1.4 GHz with the Very Large Array

⋆E-mail: dm@astro.soton.ac.uk

(VLA) (e.g. McHardyet al. 2003; Seymour et al. 2004; Loaring et al. 2005).

In this paper, we derive the 610-MHz source counts to a flux density limit (300 μJy) which is almost an order of magnitude fainter than the predicted upturn in the source counts. In this paper, the observations and data reduction are described in Section 2. The construction of the catalogue is discussed in Section 3 and we present the computation and modelling of the 610-MHz source counts in Section 4. Conclusions are presented in Section 5.

Throughout this paper, we assume a concordance cosmology with $H_0 = 70\,\mathrm{km\,s^{-1}\,Mpc^{-1}}$, $\Omega_\mathrm{M} = 0.3$ and $\Omega_\Lambda = 0.7$ (Spergel et al. 2003).

2 OBSERVATIONS AND DATA REDUCTION

In 2004 August, the 1^H field (RA = $1^\mathrm{h}45^\mathrm{m}27^\mathrm{s}$ and Dec. = $-4^\circ34'42''$) was observed for approximately 4.5 h at 610 MHz with the GMRT. Observations were carried out in dual band, spectral line mode, the former to maximize bandwidth and the latter to minimize chromatic aberration. Two sidebands, each of 128 spectral channels of 125 kHz, were centred on 602 and 618 MHz to give a total of 32 MHz bandwidth, with two independent circular polarizations recorded. Visibilities were recorded every 17 s. Observations were made of the phase calibration source 0054+035 every 45 min. The bandpass and absolute flux calibration were provided by several observations of 3C 48.

All reduction was performed with the National Radio Astronomy Observatory's AIPS software. The two sidebands were calibrated, preliminarily imaged and self-calibrated independently and then combined in the *uv* plane before final imaging. The visibilities from each baseline and channel were carefully inspected and edited to remove interference, cross-talk between antennas, instrumental glitches and the poor-quality data recorded at the beginning of each pointing.

2.1 Calibration

Absolute flux and bandpass calibration were performed in the standard way with 3C 48. Phase calibration was performed using 0054+035. Each side band underwent one cycle of phase self-calibration. We experimented with further iterations, but found that they did not improve the image quality or reduce the noise significantly. The two sidebands were then combined in the *uv* plane using the customized AIPS task UVFLP.[1]

2.2 Imaging strategy

Imaging was performed over a five by five grid of 1024 × 1024 arcsec^2 facets, with the phase of the data shifted to the tangent point at the centre of each facet. This strategy was chosen to ensure that no point on any image would be more than 10 arcmin from a tangential pointing position, minimizing the smearing of sources far from the phase tracking centre (due to the breaking of the coplanar array assumption).

The 256 channels were combined into one *uv* plane during the gridding process, imaged and deconvolution performed with the AIPS task IMAGR. The final 25 image facets used for analysis were total intensity maps, with pixel size of 1 × 1 arcsec^2. Made with a natural weighting, the central rms noise level achieved was 60 μJy with a restoring beam of 7.3 × 6.1 arcsec^2. Areas of slightly higher rms noise surround the brightest five sources, the slightly extended structures of which are imperfectly deconvolved.

Special care was taken to remove the effects of bright sources located within the side lobes of the primary beam. Small images were made of all surrounding sources found at 1.4 GHz in the NRAO VLA Sky Survey (NVSS, Condon et al. 1998), including them in the cleaning process to ensure that their side lobes were properly removed from the science images.

The maps of the individual facets were combined into a final mosaic using the AIPS task FLATN, with no correction made for the degradation of the primary beam sensitivity at this stage.

3 CATALOGUE CONSTRUCTION

3.1 Source extraction

Sources were extracted with the AIPS task SAD. A conservative peak flux density detection limit of 5σ (i.e. 300 μJy) was used to minimize the number of noise spikes spuriously detected as sources. In the areas surrounding the five brightest sources, detection was performed separately with higher detection thresholds to account for the higher rms noise. Within the 20 per cent power radius of the GMRT primary beam at 610 MHz (32 arcmin), 213 sources were discovered above a 5σ peak flux density detection limit of 300 μJy. In order to determine the success of the SAD source extraction, both the science images and the residual noise maps were carefully inspected. There were eight extended sources where the Gaussian model fit by SAD inadequately described the data. The characteristics of these sources were determined using the AIPS task TVSTAT, and contour plots of them are shown in Fig. 1. Five of these appear to contain two peaks joined by extended emission, that is, double-lobe sources.

Five further pairs of sources are separated by less than 20 arcsec, and could potentially be components of a double source. However, an inspection of i'-band imaging from SuprimeCam on the Subaru Telescope and the Digitized Sky Survey (DSS) images shows that for four of these cases, separate optical counterpart candidates are present for each source of radio emission, suggesting that they are unrelated.

The emission from the two sources constituting the remaining potential double is separated by 17 arcsec and shows no sign of extention in the direction linking the two. They have been included in the catalogue separately as sources 106 and 149.

To search for further low surface brightness extended sources, a low-resolution map was made using a similar strategy to that presented in Section 2.2, but with the *uv* visibility data tapered. With a restoring beam of 12 × 12 arcsec^2, and an rms noise of 72 μJy, 10 further sources were discovered above 5σ and added to the catalogue.

3.2 Resolution

In the analysis of low signal-to-noise ratio (S/N) detections, noise spikes can cause Gaussian fitting routines such as SAD to poorly fit the width of a source, and hence inaccurately measure the total flux density. The ratio of the total to peak flux density ($S_\mathrm{tot}/S_\mathrm{P}$) is often used to probe this effect. In Fig. 2, we plot $S_\mathrm{tot}/S_\mathrm{P}$ against S_P. Under

[1] Provided by Dave Green, http://www.mrao.cam.ac.uk/∼dag/.

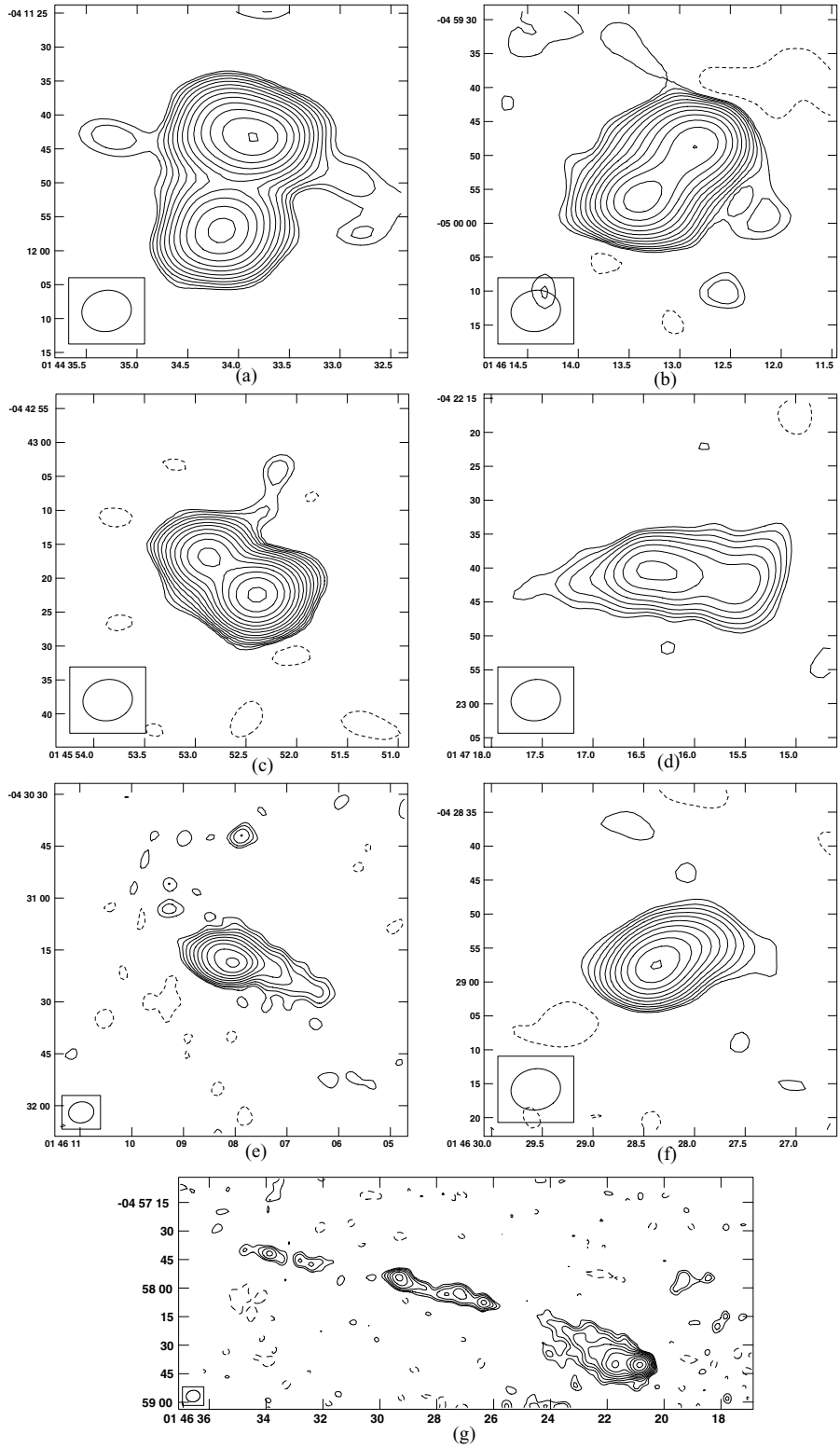

Figure 1. Plots of the contours of radio emission from sources 1, 5, 8, 16, 23 and 24 are shown in panels a, b, c, d, e and f, respectively. Panel g shows sources 10 (consisting of the two elongated patches of emission in the middle and top left-hand panels) and 20 (to the bottom right-hand panel). Contours are shown at -2, and at $2^{1+n/2}$ (where $n = 1, 2, 3\ldots$) times the local noise.

the assumption that the measurement of any source as having $S_{\rm tot} < S_{\rm P}$ is due to the effect of noise, we use the distribution of $S_{\rm tot}/S_{\rm P}$ to define a criterion for a source to be considered resolved. We define an envelope that contains 98 per cent of the sources with $S_{\rm tot}/S_{\rm P} < 1$ as $S_{\rm tot}/S_{\rm P} = 0.88^{2.5/S_{\rm P}}$, where $S_{\rm P}$ is measured in mJy. This envelope is then mirrored about $S_{\rm tot}/S_{\rm P} = 1$. Any source within this envelope is considered unresolved, and its peak flux density taken as the best measure of its true flux density.

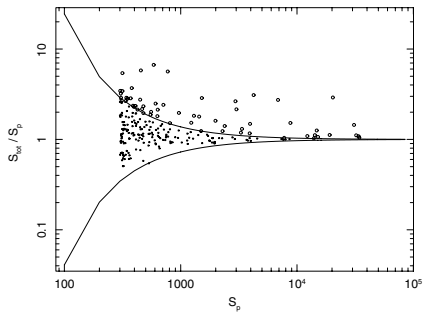

Figure 2. The ratio of $S_{\rm tot}$ to $S_{\rm P}$ as a function of $S_{\rm P}$. The solid lines indicate the upper and lower envelopes of the flux ratio distribution used to define an unresolved source. The open circles are those sources considered resolved, while the dots indicate those considered unresolved.

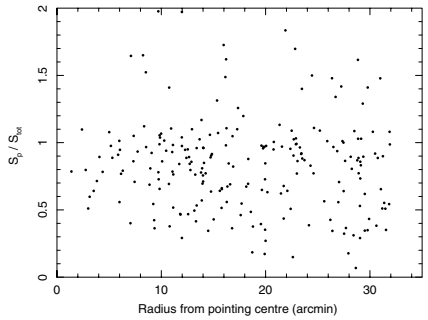

Figure 3. The variation of $S_{\rm P}/S_{\rm tot}$ across the primary beam. Any time or bandwidth smearing affecting the data would manifest itself as a decline of the $S_{\rm P}$ to $S_{\rm tot}$ ratio with radius, which is not seen.

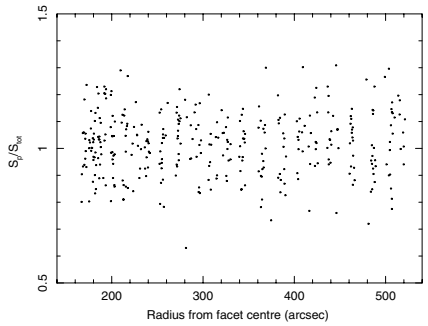

Figure 4. The ratio of $S_{\rm P}$ to $S_{\rm tot}$ for simulated sources, plotted against radial distance from the local facet tangent pointing centre at radii where any effect, if present, would be most notable. If 3D smearing were important, $S_{\rm P}/S_{\rm tot}$ would show a decrease with radius from the local pointing centre.

3.3 Flux density corrections

There are a number of potential systematic effects which can cause erroneous measurements of flux density in deep radio observations. We evaluate the impact of each as follows.

3.3.1 Bandwidth smearing

Bandwidth smearing is the result of channels of finite bandwidth being used in an interferometric inversion that assumes monochromatic radiation. Bandwidth smearing manifests itself as a radial blurring where the total flux density of a source is conserved, but the peak flux density is reduced. The effect increases with distance from the phase tracking centre. Our strategy of keeping the 128 channels of each sideband separate until the *uv* gridding process ensured minimal bandwidth smearing, as the bandwidth over which this effect is relevant is the channel width of 125 kHz rather than the total sideband bandwidth of 16 MHz. Following chapter 18 of Taylor, Carilli & Perley (1999), and approximating the *uv* coverage to a Gaussian tapered circle, and the bandpass as square, the maximal theoretical effect of bandwidth smearing (at the edge of the survey area) for our data is $|(S_{\rm P} - S_{\rm P}^{\rm true})/S_{\rm P}^{\rm true}| < 0.0003$, where $S_{\rm P}$ is the measured peak intensity and $S_{\rm P}^{\rm true}$ is the true, unsmeared peak flux density. Thus, bandwidth smearing is not considered further.

3.3.2 Time-delay smearing

Sources rotate in the sky during the 17-s integration of each of our visibilities. In the simplified case of a target at a celestial pole, the effect is essentially a smearing of each source in a direction tangential to that towards the phase tracking centre. In this simplified case and approximating to a circular *uv* coverage with Gaussian tapering (again following Taylor et al. 1999), the *maximum* theoretical effect at the edge of our survey area is a decrease in peak flux density of 4 per cent, which for the majority of sources, is smaller than the flux density measurement uncertainties.

Fig. 3 shows the ratio of measured peak to measured total flux density of the observed sources. There is no apparent dependence of this ratio on radial distance from the phase tracking centre, as would be apparent should either of these smearing effects be important. A Pearson's correlation test gives a value of -0.07, implying no significant correlation. This result confirms that neither bandwidth nor time-delay smearing has a significant effect on the quality of our images, and hence neither effect was considered further.

3.3.3 3D smearing

Sources far from the tangential pointing have their flux smeared out due to the inaccuracy of the assumption of a coplanar array in the interferometric Fourier transform relation. Our imaging strategy was expected to minimize this effect, but simulations were carried out to discover the magnitude of any remaining 3D smearing. A series of fake point sources were inserted into our *uv* coverage at a constant radius from the phase tracking centre of the field. This strategy isolates 3D smearing across a facet from the radially dependent bandwidth and time-delay smearing across the primary beam. These modified *uv* data were then imaged with the same strategy as used for the science images. The ratio of $S_{\rm P}$ to $S_{\rm tot}$ of these fake sources showed no dependence on distance from the local facet tangential pointing centre, as seen in Fig. 4. A Pearson's correlation test gives 0.03, indicative of no significant correlation. This result confirms that 3D smearing is not important, and so it is not considered further.

3.3.4 Clean bias

The Clean algorithm used to deconvolve the dirty beam can, in presence of noise, reduce the measured flux of sources. The superposition of a noise spike with a sidelobe from a real source can lead to the placing of clean components at positions not occupied by real sources. The removal of the dirty beam from this position can then remove flux from real sources and lead to systematic underestimation of their flux densities (Condon et al. 1998; Prandoni et al. 2000a; Huynh et al. 2005). To quantify the effect of this Clean

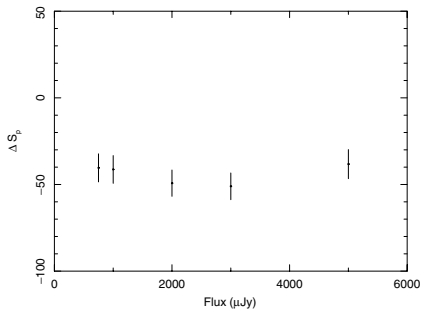

Figure 5. The average measured decrease in total flux density, for model sources inserted into the *uv* data, imaged and detected by SAD, as a function of peak flux density. Error bars give the uncertainty on the determination of the mean.

bias on our measurements, a series of fake sources with known flux densities were inserted randomly into the full *uv* data at positions not coincident with any real sources, and away from the areas of high noise surrounding the brightest sources. Imaging was then conducted in a manner similar to that used for the science images, and source extraction repeated. The measured flux densities of these model sources were then compared to the input model source parameters and the average offset as a function of flux is shown in Fig. 5. The average measured offsets are consistent with the errors on the determination of the mean at each flux. The fitting of a simple constant to the offsets at these fluxes gives 44 μJy as the amount by which the imaging, cleaning and source extraction processes have reduced the true model source flux densities. The flux densities of the real sources have been corrected, thus, before any correction for the degradation in sensitivity of the primary beam.

3.3.5 Primary beam attenuation

Any interferometric observation is modulated by the primary beam pattern of the array elements. The flux densities of all objects were corrected for the GMRT 610-MHz primary beam response using an eighth-order polynomial provided by N. Kantharia and A. Pramesh Rao (Addendum to GMRT Technical Report R00185).

3.4 Catalogue

The full catalogue is given in Table 1, in order of descending flux density, giving: (1) source number; (2) right ascension (J2000); (3) declination (J2000); (4) detection S/N; (5) peak flux density, S_P in μJy beam^{-1}; (6) angular size in arcsec (as determined from the deconvolution of the clean beam by SAD, with the exception of the eight extended sources whose flux densities were extracted using TVSTAT, in which case we give the distance in arcsec between the 4σ contours along the line of greatest extent) for those sources considered reliably resolved; (7) integrated flux density, S_{tot} in μJy for those sources considered reliably resolved; and (8) 1σ error on S_P for point sources, or S_{tot} for those resolved.

4 SOURCE COUNTS

The source counts at 1.4 GHz have been studied extensively (e.g. Windhorst et al. 1985; Hopkins et al. 1998; Richards 2000; Seymour et al. 2004) and show a flattening of the Euclidean-normalized counts below ∼1 mJy. These GMRT observations reach the depth required to confirm or deny the existence of this 'sub-mJy' bump at lower frequency.

4.1 Completeness

To be compared meaningfully to other results and with models, several completeness corrections need to be made to convert the raw source numbers into a sky density as a function of flux density.

4.1.1 Primary beam attenuation

The dominant effect is the loss of sensitivity relative to that at the phase tracking centre due to the attenuation of the primary beam. This is corrected for in the binning process by weighting each source by the area over which it could be detected, see Section 4.2.

4.1.2 Source detection completeness

Sources are detected based on peak flux density in a map of finite noise. The detected peak flux density of a source is the superposition of its intrinsic peak flux density and any noise flux at its position. This effect can be sufficient to move the sources in and out of the flux bins that correspond to their intrinsic fluxes. The important number in terms of completeness is the net gain or loss on the number of sources in each bin and is known as Eddington bias. Since the source counts are rising steeply with decreasing flux, the number of low-flux sources scattered up is likely to be greater than the number scattered down. To correct for this effect, some knowledge of the number of sources below the detection threshold is needed (Eddington 1913). Hence, we leave the discussion of this Eddington bias, which is fairly small, until Section 4.4, after the modelling of the source counts is addressed and the source counts at flux densities below the limit of our survey can be estimated.

4.1.3 Instrumental effects

Bandwidth and time-delay smearing reduce the peak flux density of a source while conserving the total flux density. Such a reduction of peak flux density can cause a source to be missed by a peak signal source extraction. However, as was shown in Section 3.3, neither bandwidth nor time-delay smearing is important in this study, and so no corrections have been made for these effects.

4.1.4 Resolution bias

We are calculating source counts based on total flux density from a catalogue selected on peak flux density, and so some sources of intrinsic low surface brightness may be missed. As in previous deep surveys (Richards 2000; Seymour et al. 2004), we have searched tapered, low-resolution maps for such sources and a small number have already been included in the catalogue.

For any value of S_{tot}, an upper angular size limit exists whereby the peak flux density of a source of that total flux still exceeds the detection limit of the survey. Using the relation

$$\frac{S_{tot}}{S_P} = \frac{\theta_{maj}\theta_{min}}{b_{maj}b_{min}}, \quad (1)$$

where θ_{maj} and θ_{min} are the major- and minor-axes of the detected source, respectively, and b_{maj} and b_{min} are the major- and minor-axes

Table 1. The complete catalogue of sources. Source number, RA, Dec., detection S/N, peak flux density, S_P, in μJy beam^{-1}, angular size in arcsec (see Section 3.4), integrated flux density, S_{tot}, in μJy, both for sources considered reliably resolved, and for σ_S, the error on the best determination of the flux density, in μJy.

Source	RA	Dec.	S/N	Peak (μJy beam^{-1})	θ (arcsec)	S_{tot} (μJy)	σ (μJy)
1[a]	01:44:34.0	−04:11:50.2	338.9	55 383.1	32.0	160 804.3	450.6
2	01:47:15.9	−04:50:09.8	537.8	138 106.8	3.73	153 572.6	285.5
3	01:44:44.3	−04:55:34.9	562.6	72 536.4	3.67	78 817.5	140.0
4	01:45:40.5	−04:12:35.0	570.5	68 278.8	2.29	71 533.8	125.3
5[a]	01:46:13.1	−04:59:53.4	114.2	20 786.1	19.51	56 590.3	453.9
6	01:43:49.2	−04:18:17.9	237.2	50 278.1	3.29	56 077.4	236.3
7	01:47:21.1	−04:45:41.6	204.4	48 648.2	3.07	52 916.9	258.8
8[a]	01:45:52.6	−04:43:19.1	515.1	35 946.5	5.16	51 873.4	99.0
9	01:45:57.8	−05:00:26.4	252.4	42 551.8	2.23	45 389.3	179.7
10[a]	01:46:21.3	−04:58:39.7	70.5	12 659.7	21.23	38 896.4	505.1
11	01:45:20.3	−05:02:00.9	126.9	22 403.5			176.4
12	01:45:32.8	−04:30:54.0	318.3	19 557.7	3.07	21 884.5	68.7
13	01:45:37.7	−04:34:00.8	246.2	14 965.6	4.27	18 768.6	74.9
14	01:46:09.6	−04:55:3.0	143.1	17 914.9			125.1
15	01:44:44.8	−04:40:26.8	232.8	16 903.4	2.5	17 331.7	74.4
16[a]	01:47:16.3	−04:22:40.7	25.3	5728.9	12.71	16 109.8	593.5
17	01:44:43.0	−04:07:45.6	65.3	13 582.1	3.13	15 794.5	241.6
18	01:45:43.7	−04:43:36.3	146.0	9982.9	7.01	15 183.6	100.5
19	01:44:14.7	−04:45:06.5	132.4	14 394.5			108.7
20[a]	01:46:29.2	−04:57:55.4	12.8	2516.3	10.24	13 578.0	1000.8
21	01:46:15.4	−04:40:29.6	129.3	9875.9	1.74	10 289.8	79.5
22	01:45:01.1	−04:59:47.7	61.3	9650.2			157.2
23[a]	01:46:08.1	−04:31:17.9	49.2	3490.1	10.51	9157.1	173.5
24[a]	01:46:28.3	−04:28:57.1	65.8	5696.1	7.38	8420.8	123.6
25	01:46:06.1	−04:35:44.2	122.2	8362.8			68.4
26	01:47:06.7	−04:53:31.5	16.0	4292.4	10.6	8233.8	487.9
27	01:47:28.4	−04:41:37.2	20.5	5334.7	7.04	8058.5	379.6
28	01:44:05.8	−04:24:36.6	9.7	1273.8	27.92	8019.3	743.1
29	01:45:14.4	−04:12:00.1	62.9	7892.5			125.4
30	01:45:20.3	−04:22:58.3	50.2	3671.0	8.67	7823.5	147.9
31	01:46:36.9	−04:43:39.7	75.7	7707.5			101.8
32	01:47:11.0	−04:50:18.3	30.9	7343.6			237.1
33	01:47:25.3	−04:43:23.2	28.0	6987.8			249.2
34	01:47:04.7	−04:49:29.2	32.0	6386.3			199.2
35	01:45:02.3	−04:12:38.6	48.6	6115.7			125.8
36	01:46:11.8	−04:16:21.7	33.1	3825.1	8.33	6099.6	177.6
37	01:43:54.2	−04:18:25.2	24.9	4888.8	3.78	6034.9	238.0
38	01:43:54.4	−04:47:44.4	35.6	5929.3			166.3
39	01:45:10.0	−04:24:22.8	56.0	4010.5	4.52	5236.4	91.8
40	01:45:52.6	−05:05:24.3	10.4	2914.3	7.85	5122.7	468.1
41	01:46:41.0	−04:25:12.2	46.3	5079.1			109.6
42	01:45:04.4	−04:03:18.8	17.0	4885.3			287.0
43	01:46:12.3	−04:37:48.5	54.8	3990.4	3.8	4732.0	86.2
44	01:45:45.1	−04:58:54.7	32.5	4681.4			143.6
45	01:46:18.4	−04:19:28.8	7.5	854.7	19.57	4588.2	548.6
46	01:44:49.1	−04:31:43.9	66.5	4584.5			68.8
47	01:46:22.2	−04:10:09.1	23.5	4581.7			194.5
48	01:44:31.4	−04:36:49.5	39.7	3148.9	6.58	4405.4	108.8
49	01:45:46.3	−04:13:41.0	37.7	4366.7			115.6
50	01:45:19.8	−04:26:20.3	65.0	4339.5			66.6
51	01:47:04.1	−04:50:55.8	18.9	4062.0			214.9
52	01:44:10.8	−04:48:12.2	31.1	4057.3			130.3
53	01:44:31.9	−04:43:27.4	24.0	2112.3	7.94	3731.1	150.1
54	01:44:32.5	−04:37:44.6	38.1	3010.3	3.61	3705.8	95.5
55	01:47:19.8	−04:42:1.0	5.0	1180.7	12.71	3694.7	677.8
56	01:45:09.3	−04:17:33.5	21.6	2042.5	7.17	3679.3	161.3
57	01:44:46.3	−05:02:24.7	5.6	1376.2	11.98	3677.6	601.7
58	01:46:15.2	−05:00:27.2	5.0	1128.4	14.81	3312.9	602.0
59	01:46:36.5	−04:24:58.0	31.4	3300.8			104.9
60	01:47:33.0	−04:32:01.3	6.1	1127.7	23.87	2991.8	540.3
61	01:45:0.0	−04:11:20.3	20.2	2878.9			141.9

Table 1 – *continued*

Source	RA	Dec.	S/N	Peak (μJy beam^{-1})	θ (arcsec)	$S_{\rm tot}$ (μJy)	σ (μJy)
62	01:46:19.5	−04:08:40.9	13.0	2841.9			217.3
63	01:46:40.3	−04:30:40.0	5.2	575.8	20.76	2804.8	485.0
64	01:45:39.5	−05:00:43.3	6.8	1230.9	19.37	2728.2	453.5
65	01:44:43.3	−04:07:55.7	12.5	2674.2			214.1
66	01:45:27.6	−04:37:41.3	7.9	1418.4	14.76	2663.0	384.4
67	01:46:02.8	−04:37:18.6	6.4	1176.6	18.44	2614.1	456.9
68	01:46:53.8	−04:36:42.2	6.6	1195.6	17.27	2589.6	444.6
69	01:44:29.9	−04:20:38.9	6.3	728.7	13.99	2490.6	362.6
70	01:44:50.1	−04:46:22.7	28.6	2357.4			82.3
71	01:46:35.5	−04:32:13.6	25.4	2339.7			91.9
72	01:44:33.1	−04:05:45.3	7.7	2334.2			302.1
73	01:46:21.8	−04:34:42.5	29.3	2310.7			78.6
74	01:45:59.7	−04:28:57.2	32.6	2277.9			69.8
75	01:46:20.8	−04:24:26.5	24.8	2245.6			90.3
76	01:46:15.5	−04:40:15.4	11.8	950.8	10.81	2210.5	175.8
77	01:45:22.1	−04:22:47.6	29.5	2190.5			74.1
78	01:46:29.5	−04:46:50.2	19.6	2078.0			105.6
79	01:47:10.9	−04:42:28.5	11.2	2037.8			177.6
80	01:43:31.5	−04:35:51.3	8.8	1913.4			216.3
81	01:47:20.4	−04:48:32.2	6.4	1886.5			279.2
82	01:46:31.8	−04:33:35.0	21.2	1869.6			87.9
83	01:46:34.2	−04:33:44.5	7.4	716.5	14.5	1859.3	232.2
84	01:44:40.9	−04:51:01.1	5.8	673.8	19.35	1770.8	283.8
85	01:45:34.2	−04:19:00.1	13.4	1185.0	5.86	1759.3	127.2
86	01:45:4.0	−05:01:42.8	8.9	1747.4			193.9
87	01:47:00.8	−04:34:13.7	12.4	1695.7			136.1
88	01:47:22.3	−04:39:01.3	7.4	1681.9			221.6
89	01:46:0.0	−04:26:13.3	10.5	814.9	8.55	1675.6	150.0
90	01:45:52.8	−04:31:50.6	10.1	695.0	9.59	1662.2	153.9
91	01:47:21.7	−04:48:40.2	5.2	1627.1			299.1
92	01:43:29.3	−04:34:40.3	6.8	1603.8			233.6
93	01:43:31.1	−04:34:44.0	7.2	1598.4			222.4
94	01:45:39.3	−04:17:21.7	7.7	772.3	10.49	1596.5	194.6
95	01:47:12.9	−04:18:27.8	5.5	1580.5			283.6
96	01:44:48.0	−04:23:13.9	7.9	703.1	8.8	1557.4	184.2
97	01:46:40.0	−04:30:04.7	5.5	610.1	12.05	1503.8	251.4
98	01:44:28.8	−05:00:52.6	5.9	1503.4			236.8
99	01:46:00.1	−04:44:57.9	9.2	753.8	8.3	1467.1	150.5
100	01:46:37.3	−04:59:47.8	5.2	1429.2			256.1
101	01:46:05.7	−04:15:14.1	11.5	1404.0			118.9
102	01:46:16.3	−04:39:58.9	9.1	753.0	8.12	1363.5	141.9
103	01:45:01.9	−04:44:55.3	5.2	433.0	11.73	1355.6	238.4
104	01:47:17.1	−04:35:01.8	6.8	1344.8			196.4
105	01:46:04.7	−05:02:57.0	5.2	1327.7			251.9
106	01:44:28.9	−04:52:11.8	9.9	1305.4			131.5
107	01:45:49.6	−04:40:50.9	19.1	1301.9			68.1
108	01:45:31.0	−04:48:40.4	15.7	1282.7			81.5
109	01:43:58.7	−04:22:23.5	8.0	1281.2			160.6
110	01:47:15.3	−04:24:21.8	5.5	1281.1			226.2
111	01:45:53.2	−04:31:24.8	19.0	1271.1			66.7
112	01:45:58.8	−05:01:00.5	6.3	1258.2			192.0
113	01:45:24.7	−04:47:28.8	16.0	1244.8			76.9
114	01:45:52.6	−04:49:07.1	6.8	1241.8			207.4
115	01:45:38.3	−04:20:28.7	5.1	462.7	9.96	1232.1	224.3
116	01:45:58.6	−04:14:52.6	10.1	1221.5			120.3
117	01:44:26.4	−04:39:23.8	6.7	1220.1			210.8
118	01:46:46.4	−04:13:43.7	5.3	1219.1			229.7
119	01:45:10.1	−04:15:22.3	11.0	1203.9			108.9
120	01:45:02.9	−05:03:35.2	6.6	1201.0			211.2
121	01:47:16.8	−04:44:22.5	5.0	1193.2			223.8
122	01:46:17.3	−04:33:52.9	7.0	577.5	8.76	1172.1	156.5
123	01:45:35.8	−04:37:49.2	6.4	1165.7			214.9
124	01:45:23.7	−04:07:44.6	6.3	1160.3			209.0

Table 1 – *continued*

Source	RA	Dec.	S/N	peak (μJy beam^{-1})	θ (arcsec)	$S_{\rm tot}$ (μJy)	σ (μJy)
125	01:45:49.0	−04:58:39.9	7.5	1155.7			151.4
126	01:44:39.5	−04:37:58.1	14.9	1142.9			76.9
127	01:46:52.3	−04:29:29.7	8.8	1114.2			125.7
128	01:46:19.0	−04:40:36.1	13.4	1113.5			81.6
129	01:46:59.1	−04:36:44.6	7.9	1084.0			136.6
130	01:45:21.2	−05:01:21.9	5.7	1069.4			187.5
131	01:46:08.3	−04:49:18.0	10.8	1064.2			98.5
132	01:46:58.8	−04:36:58.8	7.7	1052.1			134.7
133	01:45:25.1	−04:52:02.7	10.9	1049.1			95.9
134	01:46:45.2	−04:32:20.1	9.6	1045.8			105.7
135	01:45:12.7	−04:57:56.6	7.1	1022.4			142.6
136	01:45:16.9	−04:54:28.9	9.1	1017.6			109.0
137	01:44:51.8	−05:00:29.9	5.1	1015.0			199.4
138	01:44:09.8	−04:40:45.7	8.9	1011.2			109.1
139	01:45:15.3	−04:50:54.1	10.6	983.8			91.6
140	01:45:09.2	−04:47:46.8	11.9	977.4			80.8
141	01:44:46.3	−04:42:05.6	12.4	971.1			78.2
142	01:45:09.4	−04:43:31.0	13.5	970.9			71.9
143	01:46:04.2	−04:40:41.1	12.9	963.6			74.5
144	01:45:44.1	−04:58:46.1	6.0	937.6			155.8
145	01:47:08.3	−04:42:17.2	5.0	927.1			185.4
146	01:46:04.8	−04:21:27.7	10.0	922.6			91.6
147	01:45:16.3	−04:30:27.2	14.1	921.2			65.3
148	01:46:04.3	−04:39:05.6	12.2	894.3			73.2
149	01:44:29.9	−04:52:21.5	6.5	888.6			135.9
150	01:46:06.7	−04:24:49.9	10.6	882.3			81.7
151	01:44:54.2	−04:10:25.0	5.0	875.0			166.5
152	01:45:17.5	−04:34:15.9	13.5	866.8			63.9
153	01:46:13.5	−04:20:31.6	8.4	865.7			99.9
154	01:44:45.2	−04:33:39.6	10.8	799.2			74.1
155	01:45:49.1	−04:49:07.1	8.9	795.2			89.3
156	01:45:3.0	−04:34:15.2	11.7	783.5			66.9
157	01:47:01.2	−04:29:01.1	5.0	777.9			145.3
158	01:44:55.7	−04:12:17.3	5.1	775.7			149.7
159	01:44:51.1	−04:56:24.7	5.2	765.7			147.6
160	01:44:45.5	−04:27:49.5	9.5	754.6			79.0
161	01:45:26.9	−04:47:25.1	9.4	752.5			79.6
162	01:46:3.0	−04:24:09.4	8.7	736.1			83.9
163	01:45:45.2	−04:12:19.5	5.2	734.5			141.2
164	01:44:38.5	−04:45:10.6	7.9	729.9			92.1
165	01:43:58.4	−04:33:39.0	5.4	723.2			129.2
166	01:45:40.3	−04:49:5.0	8.2	721.0			84.4
167	01:45:40.5	−04:16:52.3	6.9	713.9			100.5
168	01:44:52.1	−04:55:20.6	5.2	711.7			130.1
169	01:45:04.4	−04:32:59.9	10.6	711.4			67.2
170	01:46:52.6	−04:41:48.6	5.1	704.2			138.4
171	01:46:43.7	−04:28:58.8	5.9	689.7			115.3
172	01:44:34.2	−04:26:47.4	7.4	672.7			90.2
173	01:45:03.8	−04:48:14.9	7.6	671.2			87.6
174	01:45:26.9	−04:36:05.2	10.2	658.5			63.7
175	01:45:35.1	−04:40:22.8	9.4	641.7			67.9
176	01:44:30.6	−04:34:53.1	7.3	631.5			85.8
177	01:45:44.2	−04:16:37.2	5.7	618.5			102.3
178	01:46:35.9	−04:24:21.5	5.1	609.2			118.5
179	01:44:48.5	−04:32:57.4	8.1	600.3			72.6
180	01:45:42.9	−04:36:29.8	8.9	595.7			65.7
181	01:46:45.4	−04:34:58.0	5.1	593.5			107.7
182	01:44:22.3	−04:32:55.7	6.1	588.1			95.4
183	01:46:03.1	−04:35:48.6	7.9	578.1			73.1
184	01:44:31.2	−04:37:02.2	6.4	563.5			86.4
185	01:45:56.0	−04:51:32.7	5.1	553.0			107.6
186	01:44:40.9	−04:40:03.2	6.6	545.2			82.3
187	01:45:31.5	−04:23:36.8	6.8	533.7			74.4

Table 1 – *continued*

Source	RA	Dec.	S/N	peak (μJy beam^{-1})	θ (arcsec)	$S_{\rm tot}$ (μJy)	σ (μJy)
188	01:46:12.0	−04:22:27.5	5.3	527.2			96.1
189	01:44:38.8	−04:27:44.3	5.9	516.5			83.4
190	01:44:46.8	−04:47:22.0	5.3	512.4			96.8
191	01:44:46.4	−04:48:09.8	5.0	509.7			100.3
192	01:45:31.3	−04:29:29.9	7.2	499.9			68.5
193	01:46:02.6	−04:21:52.6	5.2	496.9			91.5
194	01:45:39.5	−04:34:36.8	7.4	496.4			64.4
195	01:45:00.9	−04:38:20.4	6.8	489.7			69.8
196	01:45:53.7	−04:27:07.9	6.3	483.2			76.2
197	01:44:58.9	−04:22:38.1	5.4	482.7			85.8
198	01:44:53.1	−04:46:41.4	5.3	481.7			90.9
199	01:45:37.9	−04:32:29.5	7.1	481.1			65.2
200	01:46:06.8	−04:39:41.9	6.0	477.5			79.2
201	01:45:00.7	−04:23:31.9	5.5	470.2			84.8
202	01:46:20.5	−04:28:20.7	5.1	468.7			91.8
203	01:46:03.1	−04:44:25.9	5.4	466.6			84.5
204	01:45:22.9	−04:45:24.8	5.9	464.3			78.6
205	01:45:12.2	−04:45:08.6	5.8	463.3			78.3
206	01:44:45.2	−04:42:18.4	5.3	451.0			84.7
207	01:45:52.0	−04:44:55.0	5.3	441.4			82.5
208	01:45:19.8	−04:44:15.2	5.7	438.9			75.5
209	01:44:59.3	−04:29:05.9	5.8	434.5			73.0
210	01:44:52.9	−04:31:50.3	5.7	431.1			74.4
211	01:46:07.8	−04:30:41.9	5.4	430.6			79.8
212	01:45:19.2	−04:41:31.3	5.9	430.3			72.0
213	01:45:46.9	−04:33:17.1	6.0	418.7			69.8
214	01:45:45.1	−04:26:05.9	5.3	409.6			77.3
215	01:45:58.4	−04:37:13.3	5.4	407.0			74.4
216	01:44:52.8	−04:34:19.1	5.3	403.4			75.1
217	01:45:46.7	−04:31:16.1	5.6	400.2			68.1
218	01:45:56.8	−04:29:02.2	5.0	389.5			71.7
219	01:45:15.9	−04:41:55.6	5.2	385.1			74.2
220	01:45:40.7	−04:43:16.6	5.0	385.0			73.5
221	01:45:48.1	−04:38:09.8	5.3	383.8			71.0
222	01:45:41.3	−04:39:41.1	5.2	374.9			70.9
223	01:44:58.0	−04:36:03.1	5.0	373.8			73.8

[a]Source parameters extracted using TVSTAT.

of the restoring beam (Prandoni et al. 2000b), we calculate the size limits relevant to our full-resolution and tapered maps.

At detected fluxes above 360 μJy, the tapered map provides excellent sensitivity to the extended sources, where all sources smaller than 12 arcsec should be detected. Further, very large sources will still be missed. Due to the differing detection limits between the two maps, in the flux density range of 300 to 360 μJy, the smaller beam of the full resolution means that the sources larger than $\sim$7 arcsec are missed. Fig. 6 shows the angular size distribution of the sources in the catalogue, plotted against $S_{\rm tot}$, with the detectable size limits of both the full-resolution and the tapered maps plotted as the dashed and dotted lines, respectively. Sources whose properties place them above these limits will not be detected in our observations, and the number thereof constitutes the resolution bias. As can be seen from the angular size distribution of the detected sources, few sources would be expected to reside in the zone where resolution bias would exclude them from our catalogue.

Little is known about the angular size distribution of sub-mJy sources at 610 MHz, but the angular size distribution of the sources found in higher resolution deep surveys at 1.4 GHz over a similar flux range of 0.15 to 1 mJy (the region in 610-MHz flux space for which resolution bias may have an effect, adjusted for a spectral index of -0.7, and at sufficiently high flux that these 1.4-GHz surveys are not affected unduly by resolution bias themselves) can provide some information about the expected population. Bondi et al. (2003) fit the 1.4-GHz angular size distribution of the sources in the

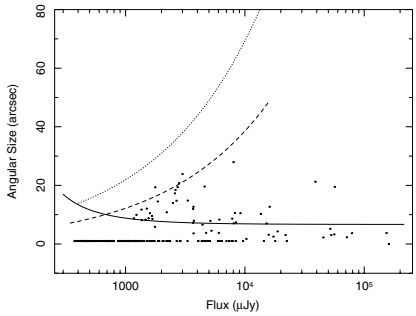

Figure 6. The angular size distribution of the sources in the 1^H field. The solid line shows the minimum size for which a source can be confidently considered resolved as a function of flux density (see Section 3.2). The dashed and dotted lines show the maximum detectable size resolution bias limits in the full-resolution and tapered maps, respectively. All sources taken as unresolved are arbitrarily plotted at 1 arcsec.

VLA-VIRMOS Deep Field over a flux range not expected to be affected by resolution bias (from 0.4 to 1 mJy). Using their formulation, we expect to miss ∼3 per cent of the sources above the tapered resolution bias limit in this flux range. Assuming this angular size distribution holds to lower 1.4-GHz flux densities, we would expect to miss only ∼7 per cent of sources which lie between the detection limits of our full-resolution and tapered 610-MHz maps. Inspecting the size distribution of sources in the 3.4-arcsec-resolution VLA A+B array 1.4-GHz map of the 13^H deep field (Seymour 2002) provides similar estimates of the fraction of sources that may be missed. Hence, we conservatively estimate the effect of resolution bias as 7 per cent below a detected flux of 360 μJy and 3 per cent between 360 μJy and 1 mJy. It should be noted that the likely steep spectrum of extended emission implies that the radius out to which an extended source could be detected is greater at 610 MHz than at 1.4 GHz, implying larger angular sizes at the lower frequency. Another limitation of examining the 1.4-GHz angular size distribution is that higher resolution images can resolve out flux from low surface brightness sources. Nevertheless, the study of the 1.4-GHz size distribution as a guide to that at 610 MHz, while not without problems, is informative.

4.2 Construction of the source counts

We have binned our sources in total flux density with the lowest bin having a lower corrected flux limit of 344 μJy. Bins of width 0.3 dex were chosen to provide good flux resolution while retaining a reasonable number of sources per bin. The highest two flux bins are widened to 0.6 dex to compensate for the lower number of sources per decade at high flux densities.

Each source was weighted by the inverse of the area over which it could have been detected – any departure from the full survey area being caused by primary beam attenuation and the areas of high rms noise surrounding the bright sources – and for the fraction of sources missed at that flux by resolution bias. These weights were then summed for all the sources in each bin, to normalize the counts expected from a Euclidean static universe, the summed weight of each bin was divided by $S_{\rm mid}^{-2.5}$, where $S_{\rm mid}$ is the flux density at the log centre of the bin. The fractional uncertainty estimates are calculated from the inverse square root of the number of sources within the bin. The bin flux limits, log bin centres, numbers of sources and normalized differential source counts (which have been corrected for Eddington bias, see Section 4.4) are tabulated in Table 2 and plotted in Fig. 7. Also plotted are the 610-MHz source counts determined from a number of Westerbork survey fields of Katgert (1979), which can be seen to agree well with the current observations. A prominent bump at sub-mJy levels, can indeed be seen at 610 MHz, where the normalized counts flatten below ∼2 mJy. Fig. 7 also includes a compilation of the source counts at 1.4 GHz (see Seymour et al. 2004, and references therein). The counts at 610 MHz follow a similar shape to those at 1.4 GHz, but with a higher normalization consistent with the sources having, on average, a steep radio spectrum. See Section 4.3 for a more detailed discussion of the relationship between the source counts in the two bands.

Table 2. Tabulated 610-MHz source counts. The columns show bin flux limits, log bin centre, number of sources and Euclidean-normalized dN/dS corrected for Eddington bias.

Bin (mJy)	$S_{\rm mid}$ (mJy)	Number	$S^{2.5}\,{\rm d}N/{\rm d}S$ (Jy$^{1.5}$ sr^{-1})
0.344–0.686	0.49	52	15.1 ± 2.6
0.686–1.34	0.97	70	15.6 ± 1.9
1.34–2.73	1.93	38	20.2 ± 3.2
2.73–5.45	3.86	25	34.4 ± 6.9
5.45–10.9	7.70	18	63.6 ± 15
10.9–43.3	21.7	11	86.5 ± 26
43.3–172	86.4	9	562 ± 187

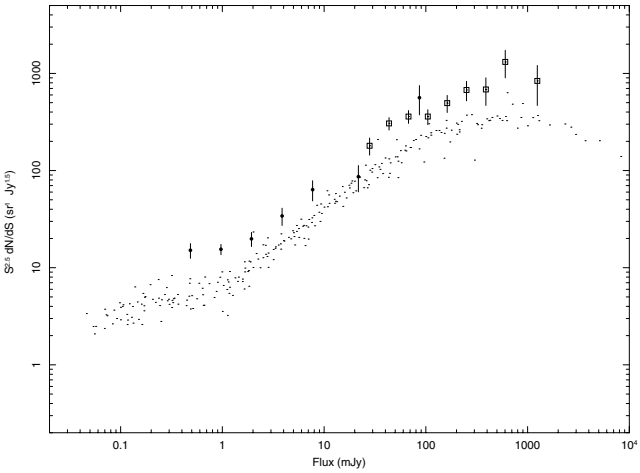

Figure 7. The differential Euclidean-normalized 610-MHz source counts as determined in the present study (filled circles), plotted at the log bin centre, $S_{\rm mid}$, and those of Katgert (1979) (empty squares) overlayed on those at 1.4 GHz (small dots) from the compilation of Seymour et al. (2004)

4.3 Modelling the 610-MHz source counts

The modelling of source counts has long been a method of constraining the cosmological evolution of radio populations, particularly those too optically faint to be spectroscopically identified (e.g. Longair 1966; Rowan-Robinson 1970; Hopkins et al. 1998; Seymour et al. 2004; Huynh et al. 2005). We model the 610-MHz source counts presented here following the method of Seymour et al. (2004) and refer the reader to their section 4.3 for details of the process. In brief, the local radio luminosity functions of both AGN and star-forming galaxies are modified by simple power-law evolution in luminosity and integrated over redshift to predict the source counts expected in deep radio surveys.

The AGN luminosity function and evolution function are taken from Rowan-Robinson et al. (1993) whose 1.4-GHz functions are based on survey work at 2.7 GHz by Dunlop & Peacock (1990). They split the local AGN population into two types, characterized by flat and steep radio spectra. In this study, the steep spectrum luminosity function was shifted to 610 MHz assuming an average spectral index of $\alpha = -0.7$. For the flat spectrum population ($\alpha = 0$) the lunimosity function at 610 MHz was taken as identical to that at 1.4 GHz.

The local starburst radio luminosity function was taken from Sadler et al. (2002), who take a sample of 242 radio sources detected in the NVSS which are identified as starburst galaxies in the 2dF Galaxy Redshift Survey. The Sadler et al. (2002) radio luminosity function was shifted to 610 MHz assuming an average spectral index of $\alpha = -0.7$, suitable for the optically thin synchrotron radiation expected from supernova remnants associated with rapid star formation. Following previous authors, the luminosity evolution was parametrized as $(1 + z)^Q$.

In order to fit this model to the 610-MHz counts and obtain useful errors on Q, we again follow the previous authors and fix the

contribution to the counts of the AGN populations. The 610-MHz source counts above ∼4 mJy are well described by the model of the combined AGN population luminosity and evolution functions as taken from Rowan-Robinson et al. (1993). Also, we assume zero density evolution, and hence the only parameter left free to vary is the power-law index of the starburst population luminosity evolution (Q). We have performed a χ^2 fit, and the best-fitting value is $Q = 2.7^{+0.15}_{-0.25}$, where the errors are given at the 1σ level.

4.4 Eddington bias and detection completeness

When source counts are rising steeply with decreasing flux density, it is likely that more sources will be scattered by the noise towards brighter fluxes than to dimmer fluxes. This effect is expected to be the greatest at the flux limit of our survey. To quantify the effect that such Eddington bias has on source counts, we use the best-fitting population model of Section 4.3 extrapolated to 60 μJy as a prediction of the source counts below the detection limit. A population of fake sources with a flux density distribution determined from this model were inserted randomly into a residual noise map. The input flux density of each source was reduced, dependent on position, to account for the attenuation of the primary beam sensitivity. Sources were then extracted from these maps and counts constructed from these detections, following the same method as used for the real sources in Section 4.2, and the process was repeated 10 times. The difference between the average detected differential source count and that of the input model gives an estimate of the *net* upscatter, that is, the Eddington bias.

Only the lowest flux bin shows a significant offset, with the average measured differential source count overestimating the inserted model value by 21 per cent. In order to make a first-order approximation to the true source counts, we therefore reduced the observed counts in the lowest flux bin by 21 per cent and refitted the model, obtaining a value of $Q = 2.45$. We note that the 21 per cent correction factor is actually slightly larger than we should be applying to return to the true source counts as it is based on an overestimate of the real value of Q, corresponding to a steeper unnormalized source count and hence to a larger number of upscattered sources than is the case in reality. However, the 21 per cent factor is not a great deal too high as we can see by repeating the simulations described above, assuming $Q = 2.45$. In this case, we find that the simulated source counts exceeded the model, in the lowest flux bin, by 19 per cent thereby almost, but not quite, returning us to our starting position. Thus, we adopt an intermediate correction factor of 20 per cent to the counts in the observed lowest flux bin which, when refitted, still provides $Q = 2.45^{+0.25}_{-0.4}$. The corrected source counts and best-fitting model are shown in Fig. 8.

An f-test gives the probability of the improvement of fit upon the inclusion of the starburst component being statistically significant at the 99.3 per cent level.

4.5 Comparison with other determinations

At 1.4 GHz and following similar methodology, Rowan-Robinson et al. (1993) find $Q = 2.5 \pm 0.5$, Hopkins et al. (1998) find $Q = 3.1 \pm 0.8$, Condon, Cotton & Broderick (2002) find $Q = 3.0 \pm 1$, Seymour et al. (2004) find $Q = 2.5 \pm 0.5$ and Huynh et al. (2005) find $Q = 2.7$. A study of *IRAS* sources believed to be tracing star-forming galaxies by Saunders et al. (1990) found evidence for luminosity evolution of $Q = 3.2 \pm 0.1$. Hopkins (2004) finds $Q = 2.7 \pm 0.60$ and $P = 0.15 \pm 0.60$ (where P is the power-law index of density evolution) as the best-fitting evolutionary scenario when both 1.4-GHz source counts and other star formation rate indicators are considered simultaneously. The best-fitting value of Q at 610 MHz ($2.45^{+0.25}_{-0.4}$) is therefore consistent, within errors, with the results from the plethora of measurements at 1.4 GHz. This agreement suggests that observations at both frequencies are probing similar source populations, and that the sources which constitute the 'sub-mJy bump' can be explained by the evolving population of starburst galaxies with steep ($\alpha \sim -0.7$) radio spectra.

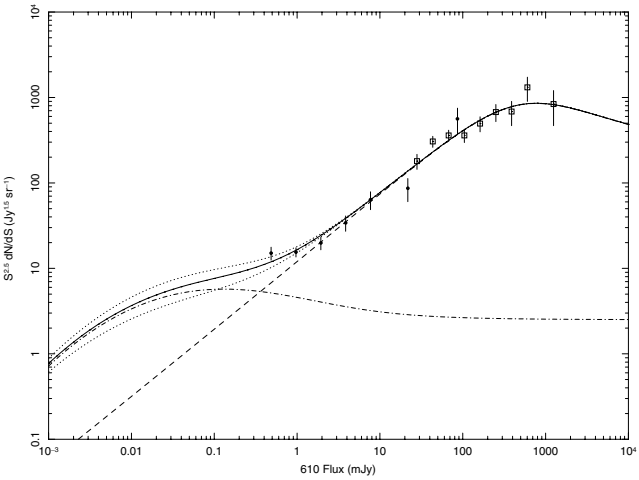

Figure 8. Model fits superposed on the 610-MHz source counts from Fig. 7. The solid line and accompanying dotted lines represent the best-fitting total model and errors. The dashed and dot–dashed lines represent the separate AGN and starburst galaxy contributions, respectively, as discussed in the text. The AGN contribution is fixed but the luminosity of the starburst contribution is allowed to evolve as $(1 + z)^Q$.

The basic two population models used here may oversimplify the true situation in faint radio sources. AGN and starburst activity can occur simultaneously in the same galaxy, and their common requirement of gas reservoirs would indicate that they are not entirely independent. However, we have shown (Seymour et al. 2004, and this work) that such a model does provide a reasonably good representation of the observed source counts at both 1.4 GHz and 610 MHz.

5 CONCLUSIONS

In an approximately 4.5-h 610-MHz observation of the 1^H *XMM–Newton*/*Chandra* 1^H survey area, 223 sources are detected down to a 5σ detection limit of 300 μJy within a 32 arcmin radius.

We confirm that the 610-MHz source counts show the upturn in Euclidean-normalized differential counts below ∼2 mJy familiar from extensive studies at 1.4 GHz. The 610-MHz counts are reasonably well fitted with a model similar to those fitted at 1.4 GHz, assuming a spectral index of $\alpha = -0.7$ for both steep spectrum AGN and a population of starburst galaxies undergoing luminosity evolution which dominate below ∼1 mJy. The best-fitting value for Q, the power-law index of the starburst luminosity evolution, is $2.45^{+0.25}_{-0.4}$. This is consistent with the determinations at 1.4 GHz.

Future deeper and wider observations at 610 MHz will improve our understanding of the source counts at this frequency. Future papers will consider the radio spectral properties of the sub-mJy radio population, which combined with other multiwavelength AGN/starburst discriminators, will allow the study of the separate evolution of the two populations.

We note that during the refereeing process, similar 610-MHz catalogues were presented by Bondi et al. (2006) and Garn et al. (2007), though neither study models the populations seen at 610 MHz.

ACKNOWLEDGMENTS

DM acknowledges the support of a PPARC studentship, and IMMᶜH and TD acknowledge the support under PPARC grant PP/D001013/1. We thank the staff of the GMRT for their very helpful support that made these observations possible. GMRT is run by the National Centre for Radio Astrophysics of the Tata Institute of Fundamental Research. DM and NSL would like to thank Niruj Mohan for indispensable advice and assistance. The DSSs were produced at the Space Telescope Science Institute under US government grant NAG W-2166. We also thank Dave Green for the customized AIPS task UVFLP, and the referee, whose comments greatly improved this manuscript.

REFERENCES

Benn C. R., Rowan-Robinson M., McMahon R. G., Broadhurst T. J., Lawrence A., 1993, MNRAS, 263, 98
Bondi M. et al., 2003, A&A, 403, 857
Bondi M. et al., 2006, A&A, 463, 873
Condon J. J., 1989, ApJ, 338, 13
Condon J. J., Cotton W. D., Greisen E. W., Yin Q. F., Perley R. A., Taylor G. B., Broderick J. J., 1998, AJ, 115, 1693
Condon J. J., Cotton W. D., Broderick J. J., 2002, AJ, 124, 675
Dunlop J. S., Peacock J. A., 1990, MNRAS, 247, 19
Eddington A., 1913, MNRAS, 73, 359
Garn T., Green D. A., Hales S. E. G., Riley J. M., Alexander P., 2007, MNRAS, 376, 1251
Hopkins A. M., 2004, ApJ, 615, 209
Hopkins A. M., Mobasher B., Cram L., Rowan-Robinson M., 1998, MNRAS, 296, 839
Huynh M. T., Jackson C. A., Norris R. P., Prandoni I., 2005, AJ, 130, 1373
Ivison R. J. et al., 2002, MNRAS, 337, 1
Katgert J. K., 1979, A&A, 73, 107
Loaring N. S. et al., 2005, MNRAS, 362, 137
Longair M. S., 1966, MNRAS, 133, 421
McHardy I. M. et al., 2003, MNRAS, 342, 802
Prandoni I., Gregorini L., Parma P., de Ruiter H. R., Vettolani G., Wieringa M. H., Ekers R. D., 2000a, A&AS, 146, 31
Prandoni I., Gregorini L., Parma P., de Ruiter H. R., Vettolani G., Wieringa M. H., Ekers R. D., 2000b, A&AS, 146, 41
Richards E. A., 2000, ApJ, 533, 611
Rowan-Robinson M., 1970, MNRAS, 149, 365
Rowan-Robinson M., Ben C. R., Lawrence A., McMahon R. G., Broadhurst T. J., 1993, MNRAS, 263, 123
Sadler E. M. et al., 2002, MNRAS, 329, 227
Saunders W., Rowan-Robinson M., Lawrence A., Efstathiou G., Kaiser N., Ellis R. S., Frenk C. S., 1990, MNRAS, 242, 318
Seymour N., 2002, PhD thesis, Univ. Southampton
Seymour N., McHardy I. M., Gunn K. F., 2004, MNRAS, 352, 131
Spergel D. N. et al., 2003, ApJS, 148, 175
Taylor G. B., Carilli C. L., Perley A. R., eds, 1999, ASP Conf. Ser. Vol. 180, Synthesis Imaging in Radio Astronomy II. Astron. Soc. Pac., San Francisco
Valentijn E. A., 1980, A&A, 89, 234
Windhorst R. A., Miley G. K., Owen F. N., Kron R. G., Koo D. C., 1985, ApJ, 289, 494

This paper has been typeset from a TEX/LATEX file prepared by the author.